Supporting Information

Control over Electron-Phonon Interaction by Dirac Plasmon Engineering in the Bi$_2$Se$_3$ Topological Insulator

Chihun In,[†] Sangwan Sim,[†,§] Beom Kim,[†] Hyemin Bae,[†] Hyunseung Jung,[∥] Woosun Jang,[‡]

Myungwoo Son,[⊥] Jisoo Moon,[#] Maryam Salehi,[▽] Seung Young Seo,[⊕] Aloysius Soon,[‡] Moon-Ho

Ham,[⊥] Hojin Lee,[∥] Seongshik Oh,[#,○] Dohun Kim,[◆] Moon-Ho Jo,[§,¶,⊕] and Hyunyong Choi,[†]*

[†]School of Electrical and Electronic Engineering and [‡]Department of Materials Science and
Engineering, Yonsei University, Seoul 03722, Republic of Korea

[§]Center for Artificial Low Dimensional Electronic Systems, Institute for Basic Science (IBS),
Pohang 37673, Republic of Korea

[∥] School of Electronic Engineering, Soongsil University, Seoul 06978, Republic of Korea

[⊥]School of Materials Science and Engineering, Gwangju Institute of Science and Technology
(GIST), Gwangju 61005, Republic of Korea

#Department of Physics and Astronomy, ▽Department of Materials Science and Engineering, and °Institute for Advanced Materials, Devices and Nanotechnology, Rutgers University, Piscataway, New Jersey 08854, United States

◆Department of Physics and Astronomy, Seoul National University, Seoul 08826, Republic of Korea

¶Division of Advanced Materials Science and ⊕Department of Materials Science and Engineering, Pohang University of Science and Technology (POSTECH), Pohang 37673, Republic of Korea

Corresponding Author

*E-mail: hychoi@yonsei.ac.kr

SA.   Sample preparation

SB.   Equations for spectral fitting

SC.   Spectral fitting results at equilibrium

SD.   2D plasmon dispersion at equilibrium

SE.   Spectral fitting results at non-equilibrium

SF.   2D plasmon dispersion at non-equilibrium

SG.   Hyperbolic plasmon–phonon polaritons

SH.   Phonon Landau damping

SI.   Hot phonon dynamics

SJ.   Fit constants

SA. Sample preparation

High-quality Bi_2Se_3 thin films were grown on 3-inch Al_2O_3 wafers (2-side polished) at Rutgers University using a custom-built MBE system (SVTA) with a base pressure lower than 5×10^{-10} Torr. The wafers were cleaned ex situ by UV-generated ozone and in situ by heating to $750\ ^\circ C$ under 10^{-6} Torr of oxygen. Using a two-temperature growth process developed at Rutgers University[1], three quintuple layers of Bi_2Se_3 were deposited at $135\ ^\circ C$ as a seed, and the rest of the film was deposited at $300\ ^\circ C$. The flux ratio of Se to Bi was maintained at above 10:1 to minimize the number of Se vacancies. After growth, the films were taken out of the vacuum chamber, immediately sealed in vacuum bags, and shipped to Yonsei University.

The slit and rod arrays on the thin films were patterned by AZ5214 with a thickness of 1.5 mm, followed by baking at $90\ ^\circ C$ for 1 min. The patterns were etched by a reactive ion etcher (40 s.c.c.m., SF6, 10 mTorr, and 45 W) with an etching rate of 18 nm/min. After the fabrication, the AZ5214 was removed with acetone.

SB. Equations for spectral fitting

We engineered the TI 2D Dirac plasmons such that the plasmon quasi-resonance spectrally overlaps with the α mode phonon. The mixed state of the two distinct resonant species leads to a well-established Fano resonance[2–5]. To extract the bare plasmon and phonon resonances from the Fano spectra, we employed the following Fano formula which is used to fit the THz extinction. Following Giannini *et al.*,[2,3] the shape of the Fano resonance associated with coupling of the plasmon and phonon resonances is described by the following equation:

$$F(\nu) = \frac{(\nu'+q)^2}{\nu'^2+1}\cdot g^2 L_{pl}(\nu).\quad (1)$$

Here, q is the shape parameter that results in the asymmetry of the Fano resonance, ν' is the reduced frequency, g is the degree of coupling between incident photons and plasmons, and $L_{pl}(\nu)$ is the bare plasmon resonance given by

$$L_{pl} = \frac{1}{1+\left(\dfrac{\nu-\nu_{pl}}{\Gamma_{pl}/2}\right)},\quad (2)$$

where v_{pl} and Γ_{pl} are the bare plasmon frequency and the plasmon linewidth, respectively. We introduce the coupling constant between the incident photon and phonon as w and the coupling constant between the phonon and the plasmon as v (see Fig. 1(c) in the main text); then, q and v' are linked to v, w, and g through

$$q = \frac{\text{v} \cdot w / g}{\Gamma_{ph}(v)/2} + \frac{v - v_{pl}}{\Gamma_{pl}/2}, \quad (3)$$

$$v' = \frac{v - v_{ph}}{\Gamma_{ph}(v)/2} - \frac{v - v_{pl}}{\Gamma_{pl}/2}, \quad (4)$$

where v_{ph} is the phonon frequency, and $\Gamma_{ph}(v) = 2\pi \cdot \text{v}^2 L_{pl}(v)$ is the phonon linewidth under Fano interference. While $F(v)$ determines the intrinsic Fano resonance, the experimentally measured THz extinction requires a fitting equation of a more complex form to account for the absorption of the incident photons by bare plasmons and phonons. According to eqs 1, 3, and 4, $F(v) = 0$ when $v = v_{ph} - \text{v} \cdot w/g$. However, since $E(v) > 0$ for all of our Tis, there must be significant absorption of photons by bare plasmons and phonons[3]. Therefore, our fitting equation has the following form:

$$E(v) = AF(v) + Bg^2 L_{pl}(v) + Cw^2 L_{ph}(v), \quad (5)$$

where A, B, and C are the fit constants for the Fano resonance, bare plasmon absorption, and bare phonon absorption, respectively. Here, the bare phonon resonance is given by

$$L_{ph} = \frac{1}{1 + \left(\dfrac{v - v_{ph}}{\Gamma_{ph}/2}\right)}, \quad (6)$$

where $\Gamma_{ph} \approx 2\pi \cdot \text{v}^2$ is the phonon linewidth without the Fano interference. The results of fitting with eq 5 are shown in Fig. 1(b) in the main text, with individual extinction components of $AF(v)$, $Bg^2 L_{pl}(v)$, and $Cw^2 L_{ph}(v)$ shown in Figs. S1 and S2 in Sec. C. We note that the bare plasmon spectral peak presented in Fig. 1(b) in the main text is given by $(A+B) \cdot g^2 L_{pl}(v)$. The pump-induced changes in the THz extinction spectra $\Delta E(v)$ shown in Fig. 2(b) and Fig. 3(b) in the main text are also fitted with eq 5.

SC. Spectral fitting results at equilibrium

In Figs. S1 and S2, we show the fits for TI slits and rods presented in Fig. 1(b) in the main text. The fits are composed of a Fano resonance $AF(\nu)$, bare plasmon absorption $Bg^2 L_{pl}(\nu)$, and bare phonon absorption $Cw^2 L_{ph}(\nu)$, as explained in Sec. B. While the Fano resonance accounts for the weakly asymmetric shape of $E(\nu)$, the broad non-zero $E(\nu)$ is associated with the bare plasmon and phonon absorption. When fitting the data for different L, we used parameters v, w, g, A, B, and C with little variation. The resulting fit constants are listed in Tables S1 and S2 in Sec. J.
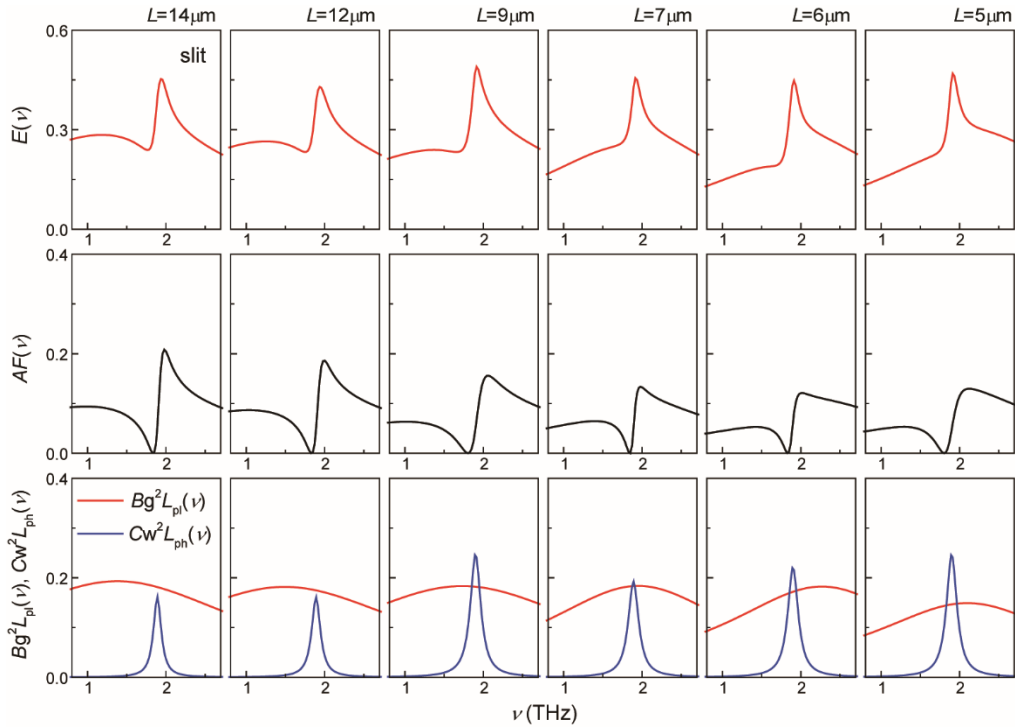
Figure S1. $E(\nu)$ fit spectra for TI slits with L varying from 14 μm to 5 μm are presented in the first row. $AF(\nu)$ is obtained using eq 5 and shown in the second row; the spectra in the third row correspond to $Bg^2 L_{pl}(\nu)$ (red line) and $Cw^2 L_{ph}(\nu)$ (blue line).

As the length L decreases, the spectral reshaping of the $Bg^2 L_{pl}(\nu)$ component implies a blue-shift of ν_{pl} (see Fig. 1(d) in the main text). Unlike graphene[6] or metal nanoparticles[7], the edge scattering of plasmons via electron–electron interaction is not significant for our TI 2D Dirac plasmons[8]. For slits (rods), we obtained the average plasmon width of $\Gamma_{pl} = 3.5 \pm 0.5\,\text{THz}$

$(2.5 \pm 0.5\,\text{THz})$. We note that the TI phonon resonance barely shows any L-dependence ($\nu_{\text{ph}} \approx 1.89\,\text{THz}$ and $\Gamma_{\text{ph}} \approx 0.16\,\text{THz}$ for both slits and rods), which indicates that the Landau damping of phonons through plasmon extinction is not efficient without optical excitation. We find that the fit value $\Gamma_{\text{ph}} \approx 0.16\,\text{THz}$ is consistent with the theoretical values of the plasmon width derived from the relationship $\Gamma_{\text{ph}} \approx 2\pi \cdot \text{v}^2$ in Sec. B. The Fano coupling parameter $\text{v} \approx 0.16\,\text{THz}^{1/2}$ used in the fitting equations leads to $\Gamma_{\text{ph}} \approx 0.16\,\text{THz}$.
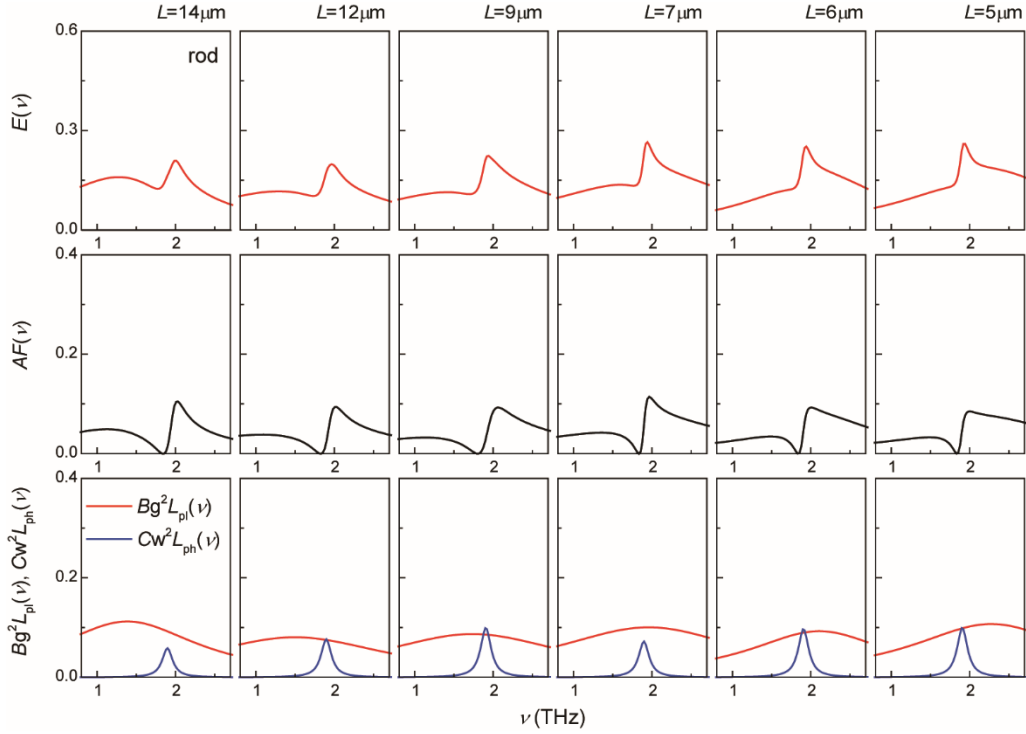
Figure S2. $E(\nu)$ fit spectra and $AF(\nu)$ for TI rods with L varying from 14 μm to 5 μm are shown in the first and second rows, respectively. The third row shows $Bg^2 L_{\text{pl}}(\nu)$ (red line) and $Cw^2 L_{\text{ph}}(\nu)$ (blue line).

SD. 2D plasmon dispersion at equilibrium

To examine the $v_{\text{pl}} \propto \sqrt{k}$ relationship illustrated in Fig. 1(d) in the main text, we consider the TI 2D plasmon dispersion where massless Dirac fermions and massive two-dimensional electron gas (2DEG) particles coexist[9–11],

$$\left(2\pi v_{\text{pl}}\right)^2 = \frac{g_s g_v k e^2}{8\pi\varepsilon_0 \hbar^2} \cdot \frac{\varepsilon_{\text{TI}}\left(E_{\text{F,T}} + E_{\text{F,B}}\right) + kz\left(\varepsilon_{\text{T}} E_{\text{F,B}} + \varepsilon_{\text{B}} E_{\text{F,T}}\right) + \sqrt{R}}{\varepsilon_{\text{TI}}\left(\varepsilon_{\text{T}} + \varepsilon_{\text{B}}\right) + kz\left(\varepsilon_{\text{TI}}^2 + \varepsilon_{\text{T}}\varepsilon_{\text{B}}\right)} . \quad (7)$$

Here, $g_s = 1$ and $g_v = 1$ are the spin and valley degeneracies of the TI Dirac surface state, $\varepsilon_{\text{TI}} = 100$ is the TI dielectric constant[4], $\varepsilon_{\text{T}} = 1$ ($\varepsilon_{\text{B}} = 10$) is the dielectric constant above (below) the top (bottom) TI surface, $E_{\text{F,T}}$ ($E_{\text{F,B}}$) is the Fermi energy of the top (bottom) TI surface, and z is the thickness of the TI thin film[4]. For slits (rods), $z = 25$ nm (15 nm); we found that a change of z by 10 nm barely changes the plasmon dispersion. The parameter R in eq 7 has the following form:

$$R = \varepsilon_{\text{TI}}^2\left(E_{\text{F,T}} + E_{\text{F,B}}\right)^2 - 2kz\varepsilon_{\text{TI}}\left(E_{\text{F,T}} - E_{\text{F,B}}\right)\left(\varepsilon_{\text{T}} E_{\text{F,B}} - \varepsilon_{\text{B}} E_{\text{F,T}}\right) + \left(kz\right)^2\left(\varepsilon_{\text{T}} E_{\text{F,B}} - \varepsilon_{\text{B}} E_{\text{F,T}}\right)^2 . \quad (8)$$

The effective Fermi energy is determined by the linear combination of the Dirac Fermi energy $E_{\text{F}}^{\text{Dirac}}$ and 2DEG Fermi energy $E_{\text{F}}^{\text{2DEG}}$ as follows,

$$E_{\text{F,i}} = E_{\text{F,i}}^{\text{Dirac}} + 4 E_{\text{F,i}}^{\text{2DEG}} \quad (\text{i} = \text{T}, \text{B}), \quad (9)$$

where the subscript $\text{i} = \text{T}, \text{B}$ indicates the top and bottom TI surfaces, respectively. The four times higher contribution of $E_{\text{F}}^{\text{2DEG}}$ than $E_{\text{F}}^{\text{Dirac}}$ to the effective Fermi energy is due to the combined effect of two-fold spin degeneracy and parabolic dispersion of 2DEG states[10]. By fitting the plasmon dispersion presented in Fig. 1(d) in the main text with eq 7, we obtain the Fermi energies of $E_{\text{F}}^{\text{Dirac}} = 465$ meV and $E_{\text{F}}^{\text{2DEG}} = 35$ meV at equilibrium. These Fermi energies are associated with the density of Dirac electrons ($n_{\text{Dirac}} \approx 1.1 \times 10^{13}$ cm^{-2}) and the density of 2DEG ($n_{\text{2DEG}} \approx 2.2 \times 10^{12}$ cm^{-2}) obtained from

$$E_{\text{F}}^{\text{Dirac}} = \hbar v_{\text{F}} \sqrt{4\pi n_{\text{Dirac}}} , \quad (10)$$

$$E_{\text{F}}^{\text{2DEG}} = \pi \hbar^2 n_{\text{2DEG}} / m^* , \quad (11)$$

where $v_F = 6 \pm 1 \times 10^5$ m/s is the Fermi velocity of the Dirac states, and $m^* = (0.15 \pm 0.01) m_0$ is the effective mass of the 2DEG states[5].

SE. Spectral fitting results non-equilibrium

Plasmon frequency-dependent THz extinction

In this part, we discuss the fitting results for the pump-induced changes in THz extinction spectra $\Delta E(v)$ after optical excitation presented in Fig. 2(b) in the main text. The first row of Fig. S3 shows the $E(v)$ spectra with and without optical excitation, and the corresponding changes $\Delta E(v)$ are shown in the second row of Fig. S3. As discussed in the main text, the main difference in $\Delta E(v)$ for varying L appears near the 1.9 THz α mode phonon resonance, where the spectra $\Delta E(v)$ for L below $8\,\mu m$ are strongly asymmetric; such asymmetry is not observed for L above $9\,\mu m$. To fit the $\Delta E(v)$ spectra, we use an equation derived from eq 5 in Sec. B as

$$\Delta E(v) = \Delta\big[AF(v)\big] + \Delta\big[Bg^2 L_{\mathrm{pl}}(v)\big] + \Delta\big[Cw^2 L_{\mathrm{ph}}(v)\big], \quad (12)$$

where $\Delta\big[AF(v)\big]$ is the change in Fano resonance, $\Delta\big[Bg^2 L_{\mathrm{pl}}(v)\big]$ is the change in bare plasmon absorption, and $\Delta\big[Cw^2 L_{\mathrm{ph}}(v)\big]$ is the change in bare phonon absorption. The response of $\Delta\big[AF(v)\big]$ shown in the third row of Fig. S3 exhibits negative values near the α mode phonon resonance, which contributes to the sharp dip in the integrated $\Delta E(v)$. Here, we find that the change in the v-parameter does not lead to any asymmetric $\Delta E(v)$ spectra. While the broad non-zero $\Delta E(v)$ is found in $\Delta\big[Bg^2 L_{\mathrm{pl}}(v)\big]$, the response of $\Delta\big[Cw^2 L_{\mathrm{ph}}(v)\big]$ accounts for the asymmetric shape of the integrated $\Delta E(v)$ for L below $8\,\mu m$. Due to the increase in v_{ph} for L below 8 μm, an asymmetric shape of the extinction spectrum emerges near the α phonon mode. In contrast, this effect is replaced by the increase in Γ_{ph} for L above $9\,\mu m$. We list the fit constants used to fit the data in Tables S1 and S3 in Sec. J.
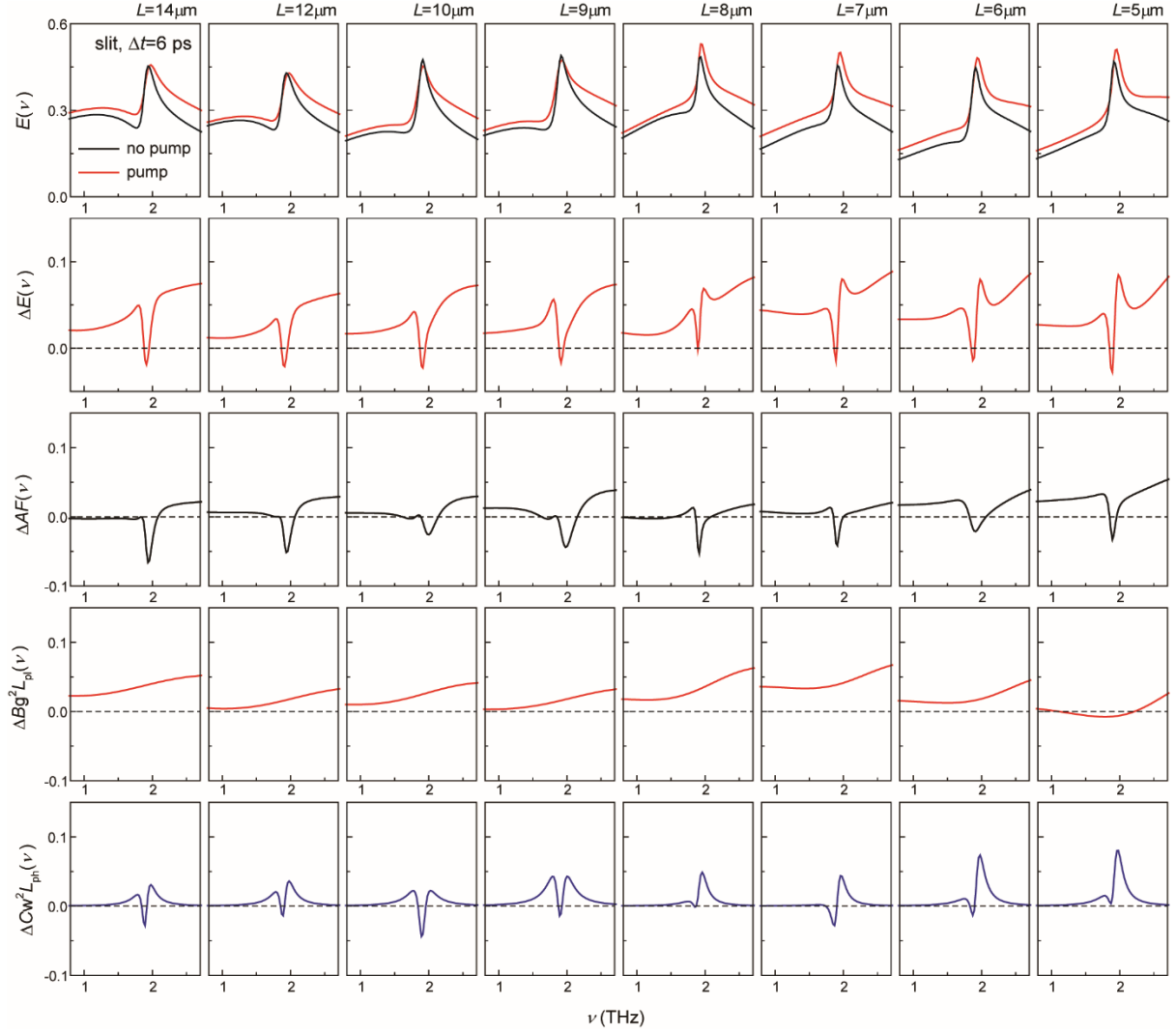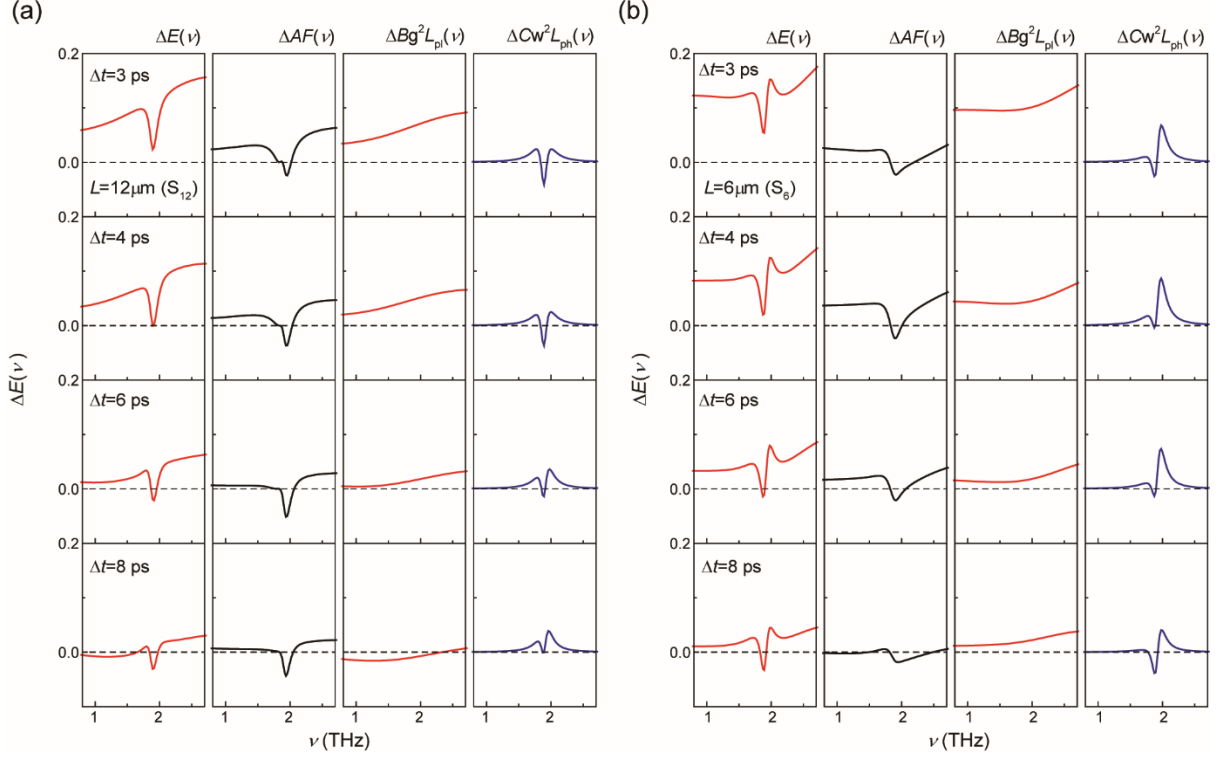
Figure S3. $E(\nu)$ spectra for TI slits at equilibrium (black line) and after optical excitation (red line) are shown in the first row. The corresponding $\Delta E(\nu)$ fit spectra are displayed in the second row. Calculated according to eq 12 $\Delta[AF(\nu)]$, $\Delta\left[Bg^2 L_{pl}(\nu)\right]$, and $\Delta\left[Cw^2 L_{ph}(\nu)\right]$ are presented in the third, fourth, and fifth rows, respectively.

Time-resolved THz extinction

In Fig. S4, the results of fitting shown in Fig. 3(b) in the main text are illustrated, where Figs. S4(a) and S4(b) represent the symmetric and asymmetric responses of the α mode phonon, respectively. Similar to $\Delta[AF(\nu)]$ in Fig. S3, the Fano interference at various Δt results in a pronounced extinction dip near the α mode phonon. While the broad non-zero spectra $\Delta E(\nu)$ are

determined by the $\Delta\left[Bg^2L_{\mathrm{pl}}(\nu)\right]$ dynamics, the symmetric or asymmetric $\Delta E(\nu)$ responses near the α mode phonon resonance are resulted from $\Delta\left[Cw^2L_{\mathrm{ph}}(\nu)\right]$. We list the fit constants in Table S4 in Sec. J.

Figure S4. $\Delta E(\nu)$ fits and detailed THz spectra at various Δt are shown for TI slits for S_{12} in (a) and for S_6 in (b).

SF. 2D plasmon dispersion at non-equilibrium

Here, we present the variation of plasmon dispersion shown in Fig. 2(c) in the main text. According to the relationships between the Fermi energies and carrier densities described in eqs 10 and 11 in Sec. D, the changes in the Dirac electron density $\Delta n_{\mathrm{Dirac}}$ and 2DEG density Δn_{2DEG} after optical excitation lead to the following changes in the Fermi level of the top TI surface:

$$E_{\mathrm{F,T}}^{\mathrm{Dirac}} = \hbar v_{\mathrm{F}}\sqrt{4\pi\left(n_{\mathrm{Dirac}} + \Delta n_{\mathrm{Dirac}}\right)}, \quad (13)$$

$$E_{\mathrm{F,T}}^{\mathrm{2DEG}} = \pi\hbar^2\left(n_{\mathrm{2DEG}} + \Delta n_{\mathrm{2DEG}}\right)/m^*. \quad (14)$$

Here, we assume that the optical pulse is predominantly absorbed by the top surface since the penetration depth (~ 20 nm) for the 800 nm pulse is smaller than the thickness of TI ($z = 25$ nm)[4]. To calculate the pump-induced carrier densities, we use the following relationships: $\Delta n_{\text{Dirac}} = F\alpha(1-r)t_{\text{Dirac}} / E_{\text{photon}}$ for Dirac states and $\Delta n_{\text{2DEG}} = F\alpha(1-r)t_{\text{2DEG}} / E_{\text{photon}}$ for 2DEG states, where $\alpha = 5\times10^5$ cm^{-1} is the absorption coefficient[12], $r = 0.5$ is the reflection coefficient[13], and $t_{\text{Dirac}} = 0.4\,\text{QL}$ ($t_{\text{2DEG}} = 4\,\text{QL}$) is the thickness of the Dirac surface (2DEG) state[13,14].

Upon optical excitation with $F = 35\,\mu\text{J/cm}^2$, the Fermi energies reach $E_{\text{F,T}}^{\text{Dirac}} = 493\,\text{meV}$ and $E_{\text{F,T}}^{\text{2DEG}} = 260\,\text{meV}$. We find that, due to the relaxation of photoinduced carriers, the Fermi energies are reduced to $E_{\text{F,T}}^{\text{Dirac}} = 480\,\text{meV}$ and $E_{\text{F,T}}^{\text{2DEG}} = 151\,\text{meV}$ at $\Delta t = 6\,\text{ps}$; this values are used to fit the plasmon dispersion in Fig. 2(c) in the main text. We obtain the dynamics of the Fermi levels using the Δt-dependent ν_{pl} in Fig. S4 in Sec. C; the corresponding Δn_{2DEG} is shown in the inset of Fig. 3(c) in the main text.

SG. Hyperbolic plasmon–phonon polaritons

In this section, we discuss why our far-field THz spectroscopy cannot provide direct experimental evidence of the hyperbolic phonon polariton (HP2) or hyperbolic plasmon–phonon polariton (HP3) modes. Following theoretical and experimental works[15,16], we first consider the HP2 mode in Bi$_2$Se$_3$ TIs with phonon resonances inside the TI slab. The angle $\theta(\omega)$ between the propagation direction and the normal to the plane is given by

$$\tan\theta(\omega) = i\frac{\varepsilon^{\perp}(\omega)^{1/2}}{\varepsilon^{z}(\omega)^{1/2}}, \quad (15)$$

where $\varepsilon^{\perp}(\omega)$ and $\varepsilon^{z}(\omega)$ constitute the following iso-frequency surfaces:

$$\frac{k_x^2 + k_y^2}{\varepsilon^{z}(\omega)} + \frac{k_z^2}{\varepsilon^{\perp}(\omega)} = \frac{\omega^2}{c^2}. \quad (16)$$

In a type-II hyperbolic region, where $\varepsilon^{z}(\omega) > 0$ and $\varepsilon^{\perp}(\omega) < 0$, the frequency dispersion of HP2 modes can be obtained as

$$k_n = -\frac{1}{d\tan\theta}\left[n\pi + \arctan\left(i\frac{\varepsilon_0}{\varepsilon_1}\right) + \arctan\left(i\frac{\varepsilon_s}{\varepsilon_1}\right)\right], \quad (17)$$

where k_n is the wavenumber with the mode index n, d is the slab thickness, ε_1 is $\varepsilon_1(\omega) = \sqrt{\varepsilon^\perp(\omega)\varepsilon^z(\omega)}$, $\varepsilon_0 = 1$ is the air permittivity, and $\varepsilon_s = 10$ is the substrate permittivity.

Using these HP2 modes, we perform numerical simulations with parameters adapted to our TI, and compare our results with those of Ref. 16. Figure S5(a) displays the HP2 modes for a TI slab thickness of $d = 120$ nm, where we see that the frequency dispersion of HP2 reproduces Fig. 4 in Ref. 16 well. Then, considering the relationship $k_n \propto d^{-1}$, decreasing d from 120 nm to 25 nm shifts the HP2 modes toward higher wavenumbers (Fig. S5(b)). In our TI geometry with $d = 25$ nm, the HP2 dispersion of k_0 is the dominant mode in the wavenumber range of our experiment (10^3 cm$^{-1} \sim 10^4$ cm^{-1}).
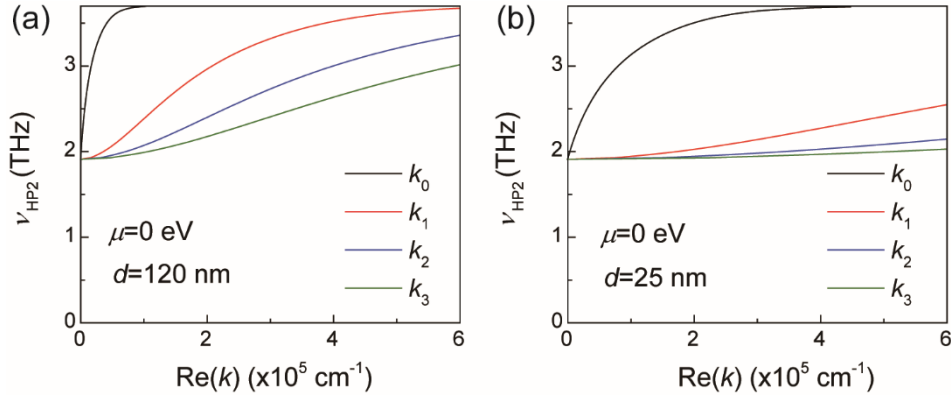
Figure S5. (a) HP2 frequency ν_{HP2} as a function of Re(k) for $\mu = 0$ eV and $d = 120$ nm. (b) ν_{HP2} as a function of Re(k) for $\mu = 0$ eV and $d = 25$ nm.

Hereafter, we discuss the hyperbolic modes for the doped surface states, i.e., HP3 modes with Dirac plasmons in the Bi$_2$Se$_3$ slab. The HP3 dispersion for $n = 0$ has the following form:

$$k_0 = -\frac{1}{d\tan\theta}\left[\arctan\left[i\frac{\varepsilon_0}{\varepsilon_1}\left(1 - 4\pi k_0\frac{\sigma_{top}}{i\omega\varepsilon_0}\right)\right] + \arctan\left[i\frac{\varepsilon_s}{\varepsilon_1}\left(1 - 4\pi k_0\frac{\sigma_{bot}}{i\omega\varepsilon_0}\right)\right]\right], \quad (18)$$

where σ_{top} and σ_{bot} are the conductance values for the top and bottom Bi$_2$Se$_3$ surfaces, respectively. In the long-wavelength limit, the sheet conductivity follows the Drude formula,

$$\sigma \cong \frac{e^2}{4\pi \hbar^2} \frac{|\mu|}{\gamma_e - i\omega}, \quad (19)$$

where μ is the Fermi energy, and $\gamma_e = 1\,\text{THz}$ is the electron scattering rate. The solutions to eqs 18 and 19 can be obtained from numerical simulations, in a form of the real and imaginary parts of the complex k_0. The simulation results are displayed in Figs. S6(a) and (c) for different Fermi energies (so that the carrier densities are different). The $\text{Re}(k_0)$ dispersion away from the phonon resonance at 1.9 THz resembles that of the surface plasmon, while a strongly dispersive feature is clearly visible near the phonon frequency ν_{ph}. These HP3 modes are expected to propagate inside the Bi$_2$Se$_3$ slab, experiencing periodic reflections at the top and bottom surfaces.
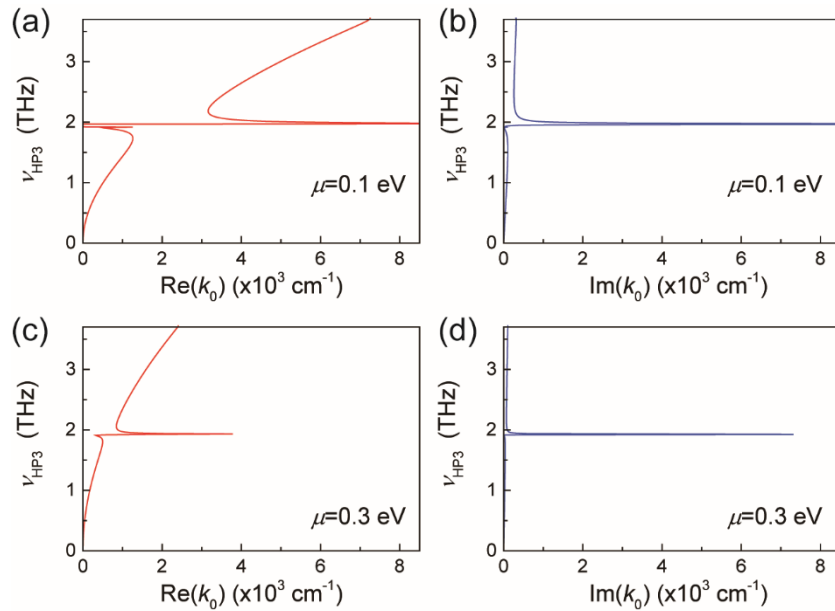
Figure S6. (a), (b) HP3 frequencies ν_{HP3} as functions of Re(k) and Im(k) for $\mu = 0.1\,\text{eV}$ and $d = 25$ nm. (c), (d) ν_{HP3} as a function of Re(k) and Im(k) for $\mu = 0.3\,\text{eV}$ and $d = 25$ nm.

It is known that one needs to employ a scattering-type near-field technique to experimentally observe the HP3 modes. This is because HP3 modes are excited by the electric field component normal to the slab orientation. Our experimental apparatus is, however, based on far-field

measurement, which limits its ability to observe the HP3 modes. Moreover, a significant damping of HP3 modes is observed near ν_{ph} in the $\text{Im}(k_0)$ dispersion curves (Figs S6(b) and (d)). This implies that the polaritonic waves near ν_{ph} barely survive inside the slab due to the increased optical loss. This consideration was also discussed in Ref. 16 in regard to s-SNOM simulations. Although it is possible that the hyperbolic HP3 modes affect our experimental data, we believe that the hyperbolic responses do not directly modify the shape of the observed change of phonon spectra near ν_{ph}.

SH. Phonon Landau damping

In this section, we use time-dependent Boltzmann's transport equations and Maxwell's equations to obtain the dispersion of phonon polaritons. The results are compared to the experimental results. Figure S7 shows the result for the phonon frequency and broadening for different Fermi energies and temperatures, while Fig. S8 shows the results for the time-dependent counterparts of the phonon frequency and broadening.

We first examine the variations of phonon polariton spectra for different Fermi levels and temperatures. Assuming that the phonon density f_{ph} fluctuates due to the external electric field $\mathbf{E} = -\nabla \phi$ with the electric potential ϕ, Boltzmann's transport equation without collisions can be written as[17]

$$\frac{\partial f_{ph}}{\partial t} + \mathbf{v}_{ph} \cdot \nabla f_{ph} - \frac{e}{m_{ph}} \mathbf{E} \cdot \nabla_v f_{e-ph} = 0. \quad (20)$$

Here, $\mathbf{v}_{ph}$ is the velocity vector of the phonon, m_{ph} is the phonon effective mass, and f_{e-ph} is the correction to the phonon velocity due to the electron–phonon interaction, which is key for deriving the phonon dispersion. Maxwell's equation can be applied to integrate f_{ph}:

$$\nabla^2 \phi = \frac{e}{\varepsilon} \int f_{ph} d^3 \mathbf{v}, \quad (21)$$

where $\varepsilon = 100\varepsilon_0$ is the Bi_2Se_3 permittivity. To solve eq 20, we assume that f_{ph} and ϕ vary periodically with $\mathbf{r}$ and t in the form of $\exp[i(\mathbf{k} \cdot \mathbf{r} - \omega t)]$[18], which yields

$$-i(\omega - \mathbf{k} \cdot \mathbf{v}_{ph}) f_{ph} + i\frac{e}{m_{ph}} \phi \mathbf{k} \cdot \nabla_v f_{e-ph} = 0, \quad (22)$$

and

$$-k^2 \phi = \frac{e}{\varepsilon} \int f_{ph} d^3 \mathbf{v}. \quad (23)$$

Equating eqs 22 and 23, we obtain the following phonon dispersion relation:

$$1 + \frac{e^2}{\varepsilon m_{ph} k^2} \int \frac{\mathbf{k} \cdot \nabla_v f_{e-ph}}{\omega - \mathbf{k} \cdot \mathbf{v}_{ph}} d^3 \mathbf{v} = 0. \quad (24)$$

Since eq 24 contains a pole at $\omega = \mathbf{k} \cdot \mathbf{v}_{ph}$, an integration path around the pole is necessary. To simplify the problem, we assume one-dimensional integration with $\mathbf{k} \cdot \mathbf{v}_{ph} = ku$, which modifies eq 24 as

$$1 + \frac{e^2}{\varepsilon m_{ph} k} \int \frac{\partial f_{e-ph}/\partial u}{\omega - ku} du = 0. \quad (25)$$

Eq 25 without the pole can be calculated term by term using the relationship

$$\frac{1}{\omega - ku} = \frac{1}{\omega}\left(1 + \frac{ku}{\omega} + \frac{k^2 u^2}{\omega^2} + \frac{k^3 u^3}{\omega^3} + \cdots\right), \quad (26)$$

where the integration around the pole results in a complex number $(-i\pi/k)\left(\partial f_{e-ph}/\partial u\right)_{u=\omega/k}$.

Hence, eq 25 can be solved as

$$1 + \frac{e^2}{\varepsilon m_{ph} k}\left[\int \frac{\partial f_{e-ph}/\partial u}{\omega}\left(1 + \frac{ku}{\omega} + \frac{k^2 u^2}{\omega^2} + \frac{k^3 u^3}{\omega^3} + \cdots\right) du - \frac{i\pi}{k}\left(\frac{\partial f_{e-ph}}{\partial u}\right)_{u=\omega/k}\right]. \quad (27)$$

To extract the phonon dispersion from eq 27, we further consider the phonon velocity correction due to the electron–phonon interaction[19],

$$f_{e-ph}(u) = \frac{n_{2DEG}}{t_{2DEG}} \frac{m^* u}{k_B T_e} \exp\left(-\frac{m^* u^2}{2k_B T_e}\right), \quad (28)$$

where n_{2DEG} is the two-dimensional electron gas density (2DEG), $t_{2DEG} = 4 \times 10^{-9}$ m is the thickness of the 2DEG, $m^* = 0.15 m_0$ is the effective mass of the 2DEG electrons, and T_e is the electron temperature. We note that eq 28 is defined on an interval of $(0, \infty)$ and reaches its maximum at the electron velocity $u = \sqrt{k_B T_e / m^*}$. Inserting eq 28 into eq 27 and integrating from 0 to ∞, we have

$$1 - \frac{\omega_0^2}{\omega^2} - k \sqrt{\frac{2\pi k_B T_e}{m^*}} \frac{\omega_0^2}{\omega^3} - 6k^2 \frac{k_B T_e}{m^*} \frac{\omega_0^2}{\omega^4} - \frac{i\pi}{k^2} \left(\frac{\partial f_{e-ph}}{\partial u} \right) = 0, \quad (29)$$

where ω_0 is defined as $\omega_0 = \sqrt{n_{2DEG} e^2 / \varepsilon m_{ph}}$. Given m_{ph} at the α phonon mode is

$m_{ph} \sim 10^7 m^{*}$ [20], we obtain the phonon dispersion relation due to the electron–phonon interaction.

Here, the change in the phonon frequency $\Delta \nu_{ph}$ is written as $\Delta \nu_{ph} = \mathrm{Re}(\omega)/2\pi$, and the change

in the phonon linewidth $\Delta \Gamma_{ph}$ corresponds to Landau damping with $\Delta \Gamma_{ph} = -\mathrm{Im}(\omega)$.
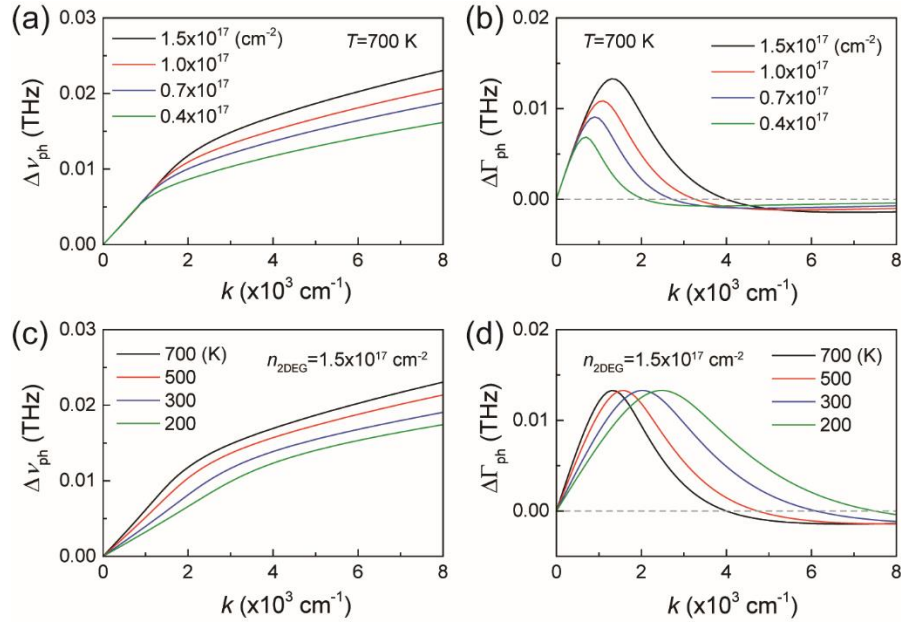
Figure S7. (a), (b) $\Delta \nu_{ph}$ and $\Delta \Gamma_{ph}$ as functions of k at different n_{2DEG}. (c), (d) $\Delta \nu_{ph}$ and $\Delta \Gamma_{ph}$ as functions of k at different T_e.

Figures S7(a) and (b) show the numerical simulation results for the carrier-density-dependent $\Delta \nu_{ph}$ and $\Delta \Gamma_{ph}$ at a fixed electron temperature of $T_e = 700\,\mathrm{K}$. We see that both $\Delta \nu_{ph}$ and $\Delta \Gamma_{ph}$ depend on k, and $\Delta \Gamma_{ph}$ increases with n_{2DEG}. Figures S7(c) and (d) depict the T_e-dependent $\Delta \nu_{ph}$ and $\Delta \Gamma_{ph}$ for a fixed n_{2DEG}. The origin of phonon Landau damping can be quantitatively understood by introducing a screening parameter called Debye length λ_D [19], which

represents the screening effect of a free electron plasma. Given that λ_D is $\sqrt{k_B T_e / m^* \omega_0^2}$, the peak of $\Delta\Gamma_{ph}$ emerges when $k = \lambda_D^{-1}$. This implies that the phonon Landau damping originates from the screening effects of the electron plasma; the oscillating phonon wave is screened by the incoherent thermal motion of free electrons.

Having discussed the effects of n_{2DEG} and T_e on the phonon dispersion relation, we now discuss the relevance of the presented theoretical analysis to our experimental observations. After optical excitation, both n_{2DEG} and T_e vary as functions of the pump-probe delay Δt. Employing Δt-dependent n_{2DEG} and T_e values from the calculations described in Fig. 3(c) in the manuscript and Supporting Information Sec. I, in Fig. S8 we show the Δt-dependent $\Delta\nu_{ph}$ and $\Delta\Gamma_{ph}$ dispersion curves. Here, we examine two key aspects of comparison between the theory and the experimental observations. Firstly, $\Delta\nu_{ph}$ increases as a function of k (Fig. S8(a)), while $\Delta\Gamma_{ph}$ significantly decreases above $k \sim 4 \times 10^3$ cm^{-1}. This indeed occurs when ν_{pl} is the same as ν_{ph} (Fig. S8(b)), which is consistent with our experimental observations shown in Fig. 2 in the manuscript. Secondly, both $\Delta\nu_{ph}$ and $\Delta\Gamma_{ph}$ relax with Δt, which accounts for the Δt-dependent data shown in Fig. 3 in the manuscript. As n_{2DEG} and T_e return to equilibrium, $\Delta\nu_{ph}$ and $\Delta\Gamma_{ph}$ decrease due to electron–phonon coupling. The simulation results are not scaled to exactly match the experimental results. This may be because we did not consider the hot phonon effect, as discussed in Supporting Information Sec. I. The main result of the simulations is that we can understand why the phonon Landau damping emerges after optical excitation and relaxes as a function of Δt through theoretical electromagnetic modeling.
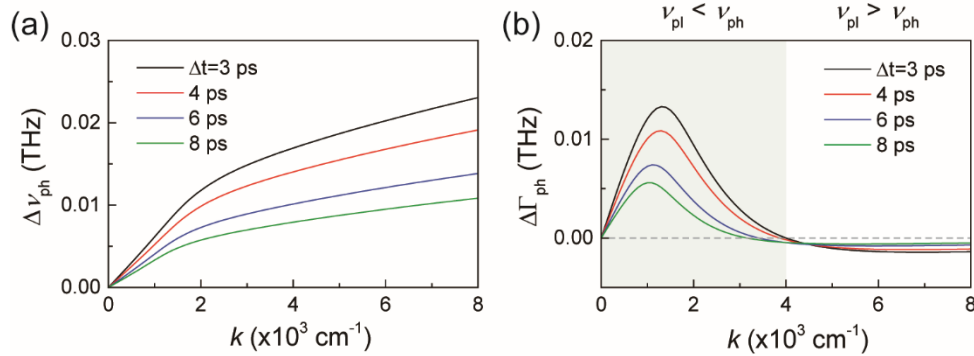
Figure S8. (a), (b) $\Delta \nu_{ph}$ and $\Delta \Gamma_{ph}$ as functions of k at different Δt. The shaded region in (b) corresponds to $\nu_{pl} < \nu_{ph}$.

To summarize, we performed numerical investigation of the phonon Landau damping based on a model of electron plasma using Boltzmann's and Maxwell's equations. The theoretical analysis qualitatively corroborates the density- and temperature-dependent experimental observations for Bi_2Se_3 plasmonic structures with given n_{2DEG} and T_e. According to our interpretation, the observed frequency and linewidth changes of the phonon polaritons arise from the screening effect of the electron plasma; further, the phonon polaritons can be engineered by changing the momentum and resonance energy of the associated Dirac plasmons.

SI. Hot phonon dynamics

Here, we inspect the hot phonon effect due to the increased lattice temperature. The relaxation dynamics of $\Delta \Gamma_{ph}$ in S_6 and S_{12} are described by exponential decay through the following equations:

$$\Delta \Gamma_{ph}(S_6) = \Delta \Gamma_{th} \exp(-\Delta t / \tau_{diff}), \quad (30)$$

$$\Delta \Gamma_{ph}(S_{12}) = \Delta \Gamma_{th} \exp(-\Delta t / \tau_{diff}) + \Delta \Gamma_{LD} \exp(-\Delta t / \tau_{LD}), \quad (31)$$

with the results presented in Fig. S9(a). We observe that optical excitation results in increase of both $\Delta \Gamma_{ph}(S_6)$ and $\Delta \Gamma_{ph}(S_{12})$ by $\Delta \Gamma_{th} \approx 0.06\,THz$ owing to the increased lattice temperature[21,22], with the corresponding decay determined by a thermal diffusion time constant $\tau_{diff} = 21\,ps$[23,24]. Eq 31 includes an additional phonon damping term with $\Delta \Gamma_{LD} \approx 0.14\,THz$, which accounts for the Landau damping of the phonon. As discussed in Sec. H, the fast decay of the Landau damping closely follows the decay of photoexcited electrons, which is characterized by the time constant $\tau_{LD} \approx 4.1\,ps$.

To systemically describe the hot phonon effect after optical excitation, we employ a two-temperature model (TTM). The results are displayed in Fig. S9(b). Upon optical excitation, the energy density absorbed by electrons is $(1-r)F/z$, where $r = 0.5$ is the reflectivity,

$F = 35\,\mu\text{J/cm}^2$ is the incident pump fluence, and $z = 2.5\times10^{-8}$ m is the film thickness. The increased electron temperature T_{e} equilibrates with the lattice temperature T_{L} through dynamic relaxation. The dynamics of T_{e} and T_{L} are simulated using the following rate equations[25]:

$$\frac{d}{dt}\left[\frac{1}{2}\gamma_{\text{e}}T_{\text{e}}^2\right] = \frac{(1-r)F\delta(t)}{z} - U_{\text{e-ph}}(T_{\text{e}},T_{\text{L}}), \quad (32)$$

$$\frac{d}{dt}\left[C_{\text{L}}T_{\text{L}}\right] = -\frac{C_{\text{L}}T_{\text{L}}}{\tau_{\text{diff}}} + U_{\text{e-ph}}(T_{\text{e}},T_{\text{L}}), \quad (33)$$

where $\gamma_{\text{e}} = 10\,\text{J m}^{-3}\,\text{K}^{-2}$ is the electron specific heat coefficient [25,26], C_{L} is the Debye phonon heat capacity, and $U_{\text{e-ph}}(T_{\text{e}},T_{\text{L}})$ is the electron–phonon energy coupling rate. The Debye model yields the following relationships[25]:

$$C_{\text{L}} = 10^{28}k_{\text{B}}\left(\frac{T_{\text{L}}}{\theta_{\text{D}}}\right)^3 \int_0^{\frac{\theta_{\text{D}}}{T_{\text{L}}}} \frac{x^4 e^x}{(e^x-1)^2}\,dx \; [\text{J K}^{-1}\,\text{m}^{-3}], \quad (34)$$

$$U_{\text{e-ph}}(T_{\text{e}},T_{\text{L}}) = 4g_{\infty}\theta_{\text{D}}\left[\left(\frac{T_{\text{e}}}{\theta_{\text{D}}}\right)^5 \int_0^{\frac{\theta_{\text{D}}}{T_{\text{e}}}} \frac{x^4}{e^x-1}\,dx - \left(\frac{T_{\text{L}}}{\theta_{\text{D}}}\right)^5 \int_0^{\frac{\theta_{\text{D}}}{T_{\text{L}}}} \frac{x^4}{e^x-1}\,dx\right], \quad (35)$$

where $\theta_{\text{D}} = 180\,\text{K}$ [26] is the Debye temperature of Bi_2Se_3, and $g_{\infty} = 2\times10^{15}\,\text{J K}^{-1}\,\text{s}^{-1}\,\text{m}^{-3}$ is the electron–phonon coupling constant. We note that the TTM is applicable for temperatures above $\theta_{\text{D}}/5 = 36\,\text{K}$ [27]; for lower temperatures, electron–electron thermalization becomes significant. In our case of $T_{\text{L}} > 78\,\text{K}$, the transient dynamics of T_{e} and T_{L} are described by the TTM reasonably well. Figure S7(b) shows the relaxation of T_{e} and T_{L} equilibrating at $\Delta t \sim 10\,\text{ps}$. We see that the decay of T_{e} is similar to that measured in angle-resolved photoemission spectroscopy (ARPES)[26]. From the increase of T_{L} above the initial value of 78 K, the contribution $\Delta\Gamma_{\text{th}}$ due to the hot phonon effect is evident.

When $T_{\text{e}}, T_{\text{L}} > \theta_{\text{D}}$, g_{∞} is directly related to the dimensionless electron–phonon coupling constant λ, which is expressed with the following equation[25],

$$g_{\infty} = \frac{3\hbar\lambda\gamma_{\text{e}}\langle\omega^2\rangle}{\pi k_{\text{B}}}. \quad (36)$$

Here, $\langle \omega^2 \rangle \approx (2.9\,\text{THz})^2$ is the second moment of the Debye phonon spectrum in Bi_2Se_3 that can be calculated as[28]

$$\langle \omega^2 \rangle = \frac{\int_0^{k\theta_D/\hbar} \omega^2 D(\omega)\, d\omega}{\int_0^{k\theta_D/\hbar} D(\omega)\, d\omega}, \quad (37)$$

where $D(\omega)$ is the phonon density of states. Using eq 36, a value of $\lambda = 0.082$ is obtained, which is consistent with the result previously measured with ARPES[29].
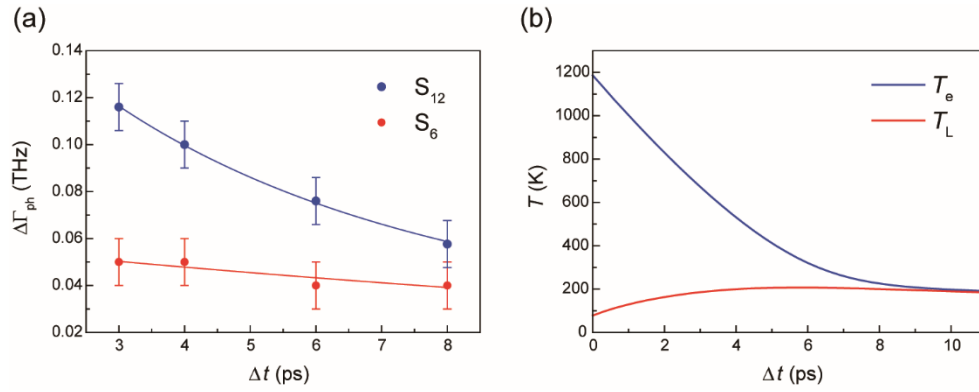
Figure S9. (a) $\Delta\Gamma_{ph}$ at different Δt are shown for S_{12} (blue dots) and S_6 (red dots). Red and blue solid lines are fits to the data obtained from eqs 30 and 31. (b) Transient responses of T_e and T_L are obtained from eqs 32 and 33.

SJ. Fit constants

Fit constants	L=14 μm	L=12 μm	L=10 μm	L=9 μm	L=8 μm	L=7 μm	L=6 μm	L=5 μm
v (THz$^{1/2}$)	0.15	0.16	0.2	0.19	0.13	0.14	0.2	0.16
w (THz)	0.15	0.15	0.19	0.2	0.15	0.17	0.2	0.18
g (THz$^{1/2}$)	0.45	0.44	0.44	0.42	0.51	0.5	0.42	0.42
v_{pl} (THz)	1.38	1.49	1.64	1.73	1.83	1.95	2.1	2.27
Γ_{pl} (THz)	4	4	4	3.5	4	3	3	3
v_{ph} (THz)	1.89	1.89	1.9	1.9	1.89	1.89	1.9	1.9
Γ_{ph} (THz)	0.16	0.16	0.16	0.16	0.16	0.16	0.16	0.16
A	0.53	0.51	0.4	0.49	0.36	0.33	0.47	0.47
B	0.95	0.92	0.88	1.06	0.79	0.73	0.85	1.03
C	7	6.7	7	6.2	7	7	6.2	7

Table S1. Fit constants for TI slits in equilibrium (Fig. S1 and Fig. S3).

Fit constants	L=14 μm	L=12 μm	L=9 μm	L=7 μm	L=6 μm	L=5 μm
v (THz$^{1/2}$)	0.19	0.18	0.2	0.14	0.15	0.15
w (THz)	0.14	0.16	0.2	0.19	0.19	0.2
g (THz$^{1/2}$)	0.5	0.41	0.39	0.44	0.44	0.45
v_{pl} (THz)	1.38	1.49	1.73	1.95	2.1	2.27
Γ_{pl} (THz)	2.2	3	3	3	2.2	2.5
v_{ph} (THz)	1.89	1.89	1.9	1.89	1.9	1.9
Γ_{ph} (THz)	0.16	0.16	0.16	0.16	0.16	0.16
A	0.23	0.28	0.30	0.3	0.29	0.28
B	0.45	0.48	0.57	0.52	0.48	0.53
C	3	3	2.5	2	2.7	2.5

Table S2. Fit constants for TI rods in equilibrium (Fig. S2).

Fit constants	L=14 μm	L=12 μm	L=10 μm	L=9 μm	L=8 μm	L=7 μm	L=6 μm	L=5 μm
v (THz$^{1/2}$)	0.18	0.18	0.23	0.24	0.13	0.14	0.2	0.16
w (THz)	0.16	0.16	0.19	0.2	0.16	0.18	0.2	0.18
g (THz$^{1/2}$)	0.45	0.45	0.44	0.45	0.52	0.52	0.49	0.49
v_{pl} (THz)	1.61	1.73	1.9	2	2.1	2.2	2.45	2.7
Γ_{pl} (THz)	5	5	4	4.5	3.6	4	3.8	3.8
v_{ph} (THz)	1.9	1.9	1.9	1.9	1.91	1.92	1.92	1.92
Γ_{ph} (THz)	0.24	0.24	0.23	0.25	0.19	0.19	0.2	0.2
A	0.53	0.56	0.46	0.5	0.36	0.33	0.47	0.54
B	0.95	0.92	0.88	1.06	0.79	0.73	0.85	1.03
C	5.2	6.1	5.6	5.8	7	5.9	6.5	8

Table S3. Fit constants for TI slits in non-equilibrium (Fig. S3).

Fit constants	L=12 μm				L=6 μm			
	Δt=3 ps	Δt=4 ps	Δt=6 ps	Δt=8 ps	Δt=3 ps	Δt=4 ps	Δt=6 ps	Δt=8 ps
v (THz$^{1/2}$)	0.18	0.18	0.18	0.18	0.2	0.2	0.2	0.2
w (THz)	0.16	0.16	0.16	0.16	0.2	0.2	0.2	0.2
g (THz$^{1/2}$)	0.49	0.46	0.44	0.46	0.48	0.53	0.49	0.42
v_{pl} (THz)	2	1.89	1.73	1.63	2.8	2.6	2.45	2.3
Γ_{pl} (THz)	5	4.7	4.9	4.8	5.7	4.7	3.8	3.3
v_{ph} (THz)	1.89	1.89	1.9	1.9	1.93	1.92	1.92	1.92
Γ_{ph} (THz)	0.25	0.234	0.21	0.19	0.21	0.21	0.2	0.2
A	0.59	0.59	0.56	0.51	0.47	0.47	0.47	0.47
B	1.02	1.04	0.96	0.786	1.16	0.73	0.74	1
C	5	5.2	6.2	6.5	6.1	6.8	6.5	5.6

Table S4. Fit constants for time-resolved THz extinction in TI slits (Fig. S4).

REFERENCES

(1)   Bansal, N.; Kim, Y. S.; Edrey, E.; Brahlek, M.; Horibe, Y.; Iida, K.; Tanimura, M.; Li, G. H.; Feng, T.; Lee, H. D.; Gustafsson, T.; Andrei, E.; Oh, S. Epitaxial growth of topological insulator Bi_2Se_3 film on Si(111) with atomically sharp interface. *Thin Solid Films* **2011**, *520* (1), 224–229.

(2)   Giannini, V.; Francescato, Y.; Amrania, H.; Phillips, C. C.; Maier, S. A. Fano resonances in nanoscale plasmonic systems: A parameter-free modeling approach. *Nano Lett.* **2011**, *11* (7), 2835–2840.

(3)   Francescato, Y.; Giannini, V.; Maier, S. A. Plasmonic systems unveiled by Fano resonances. *ACS Nano* **2012**, *6* (2), 1830–1838.

(4)   Sim, S.; Jang, H.; Koirala, N.; Brahlek, M.; Moon, J.; Sung, J. H.; Park, J.; Cha, S.; Oh, S.; Jo, M.-H.; Ahn, J.-H.; Choi, H. Ultra-high modulation depth exceeding 2,400% in optically controlled topological surface plasmons. *Nat. Commun.* **2015**, *6*, 8814.

(5)   Di Pietro, P.; Ortolani, M.; Limaj, O.; Di Gaspare, A.; Giliberti, V.; Giorgianni, F.; Brahlek, M.; Bansal, N.; Koirala, N.; Oh, S.; Calvani, P.; Lupi, S. Observation of Dirac plasmons in a topological insulator. *Nat. Nanotechnol.* **2013**, *8* (8), 556–560.

(6)   Yan, H.; Low, T.; Zhu, W.; Wu, Y.; Freitag, M.; Li, X.; Avouris, P.; Xia, F. Damping pathways of mid-intrared plasmons in graphene nanostructures. *Nat. Photonics* **2013**, *7* (5), 394–399.

(7)   Link, S.; El-Sayed, M. A. Spectral properties and relaxation dynamics of surface plasmon electronic oscillations in gold and silver nanodots and nanorods. *J. Phys. Chem. B* **1999**, *103* (40), 8410–8426.

(8)   Ou, J.-Y.; So, J.-K.; Adamo, G.; Sulaev, A.; Wang, L.; Zheludev, N. I. Ultraviolet and visible range plasmonics in the topological insulator $Bi_{1.5}Sb_{0.5}Te_{1.8}Se_{1.2}$. *Nat. Commun.* **2014**, *5*, 5139.

(9)   Stauber, T.; Gómez-Santos, G.; Brey, L. Spin-charge separation of plasmonic excitations in thin topological insulators. *Phys. Rev. B* **2013**, *88* (20), 205427.

(10)   Stauber, T. Plasmonics in Dirac systems: From graphene to topological insulators. *J. Phys. Condens. Matter* **2014**, *26* (12), 123201.

(11) Stauber, T.; Gómez-Santos, G.; Brey, L. Plasmonics in topological insulators: Spin-charge separation and the influence of the inversion layer. *ACS Photonics* **2017**, *4* (12), 2978–2988.

(12) Glinka, Y. D.; Babakiray, S.; Johnson, T. A.; Bristow, A. D.; Holcomb, M. B.; Lederman, D. Ultrafast carrier dynamics in thin-films of the topological insulator Bi_2Se_3. *Appl. Phys. Lett.* **2013**, *103* (15), 151903.

(13) Sim, S.; Brahlek, M.; Koirala, N.; Cha, S.; Oh, S.; Choi, H. Ultrafast terahertz dynamics of hot Dirac-electron surface scattering in the topological insulator Bi_2Se_3. *Phys. Rev. B* **2014**, *89* (16), 165137.

(14) Bansal, N.; Kim, Y. S.; Brahlek, M.; Edrey, E.; Oh, S. Thickness-independent transport channels in topological insulator Bi_2Se_3 thin films. *Phys. Rev. Lett.* **2012**, *109* (11), 116804.

(15) Basov, D. N.; Fogler, M. M.; Garcia de Abajo, F. J. Polaritons in van der waals materials. *Science* **2016**, *354* (6309), aag1992.

(16) Wu, J. S.; Basov, D. N.; Fogler, M. M. Topological insulators are tunable waveguides for hyperbolic polaritons. *Phys. Rev. B* **2015**, *92* (20), 205430.

(17) Stauber, T.; Peres, N. M. R.; Guinea, F. Electronic transport in graphene: A semiclassical approach including midgap states. *Phys. Rev. B* **2007**, *76* (20), 205423.

(18) Ryzhii, V.; Satou, A.; Otsuji, T. Plasma waves in two-dimensional electron-hole system in gated graphene heterostructures. *J. Appl. Phys.* **2007**, *101* (2), 024509.

(19) Rubab, N.; Murtaza, G. Debye length in non-Maxwellian plasmas. *Phys. Scr.* **2006**, *74* (2), 145–148.

(20) Kim, D.; Li, Q.; Syers, P.; Butch, N. P.; Paglione, J.; Sarma, S. Das; Fuhrer, M. S. Intrinsic electron-phonon resistivity of Bi_2Se_3 in the topological regime. *Phys. Rev. Lett.* **2012**, *109* (16), 166801.

(21) Laforge, A. D.; Frenzel, A.; Pursley, B. C.; Lin, T.; Liu, X.; Shi, J.; Basov, D. N. Optical characterization of Bi_2Se_3 in a magnetic field: Infrared evidence for magnetoelectric coupling in a topological insulator material. *Phys. Rev. B* **2010**, *81* (12), 125120.

(22) Wu, L.; Brahlek, M.; Valdés Aguilar, R.; Stier, A. V; Morris, C. M.; Lubashevsky, Y.; Bilbro, L. S.; Bansal, N.; Oh, S.; Armitage, N. P. A sudden collapse in the transport

lifetime across the topological phase transition in $(Bi_{(1-x)}In_{(x)})_2Se_3$. *Nat. Phys.* **2013**, *9* (7), 410–414.

(23)   Valdés Aguilar, R.; Qi, J.; Brahlek, M.; Bansal, N.; Azad, A.; Bowlan, J.; Oh, S.; Taylor, A. J.; Prasankumar, R. P.; Yarotski, D. A. Time-resolved terahertz dynamics in thin films of the topological insulator Bi_2Se_3. *Appl. Phys. Lett.* **2015**, *106* (1), 011901.

(24)   Sobota, J. A.; Yang, S.; Analytis, J. G.; Chen, Y. L.; Fisher, I. R.; Kirchmann, P. S.; Shen, Z. X. Ultrafast optical excitation of a persistent surface-state population in the topological insulator Bi_2Se_3. *Phys. Rev. Lett.* **2012**, *108* (11), 117403.

(25)   Lai, Y. P.; Chen, H. J.; Wu, K. H.; Liu, J. M. Temperature-dependent carrier-phonon coupling in topological insulator Bi_2Se_3. *Appl. Phys. Lett.* **2014**, *105* (23), 232110.

(26)   Wang, Y. H.; Hsieh, D.; Sie, E. J.; Steinberg, H.; Gardner, D. R.; Lee, Y. S.; Jarillo-Herrero, P.; Gedik, N. Measurement of intrinsic Dirac fermion cooling on the surface of the topological insulator Bi_2Se_3 using time-resolved and angle-resolved photoemission spectroscopy. *Phys. Rev. Lett.* **2012**, *109* (12), 127401.

(27)   Dai, Y. M.; Bowlan, J.; Li, H.; Miao, H.; Wu, S. F.; Kong, W. D.; Shi, Y. G.; Trugman, S. A.; Zhu, J. X.; Ding, H.; Taylor, A. J.; Yarotski, D. A.; Prasankumar, R. P. Ultrafast carrier dynamics in the large-magnetoresistance material WTe_2. *Phys. Rev. B* **2015**, *92* (16), 161104.

(28)   Cheng, L.; La-O-Vorakiat, C.; Tang, C. S.; Nair, S. K.; Xia, B.; Wang, L.; Zhu, J. X.; Chia, E. E. M. Temperature-dependent ultrafast carrier and phonon dynamics of topological insulator $Bi_{1.5}Sb_{0.5}Te_{1.8}Se_{1.2}$. *Appl. Phys. Lett.* **2014**, *104* (21), 211906.

(29)   Pan, Z. H.; Fedorov, A. V.; Gardner, D.; Lee, Y. S.; Chu, S.; Valla, T. Measurement of an exceptionally weak electron-phonon coupling on the surface of the topological insulator Bi_2Se_3 using angle-resolved photoemission spectroscopy. *Phys. Rev. Lett.* **2012**, *108* (18), 187001.